ORIGINAL ARTICLE

A modified energy-based fatigue parameter for short fiber reinforced polymers: Performance analysis with varying thicknesses, load ratios, and fiber orientations

Francesco E. Fiorini[1,2] | Luca M. Martulli[2] | Philippe Steck[1] | Andrea Bernasconi[2]

[1]Competence Center Mechanics, thyssenkrupp Presta AG, Eschen, Principality of Liechtenstein

[2]Department of Mechanical Engineering, Politecnico di Milano, Milan, Italy

Correspondence
Francesco E. Fiorini, Competence Center Mechanics, thyssenkrupp Presta AG, Essanestrasse 10, 9492 Eschen, Principality of Liechtenstein.
Email: francesco.fiorini@thyssenkrupp-automotive.com

Abstract

The durability of short fiber reinforced polymers (SFRPs) is affected by several variables. Accurate unifying fatigue parameters are thus essential for an efficient characterization campaign. This research investigated the fatigue behavior of a Polyphtalamide PA6T/6I reinforced with 50% of glass fibers. Two thicknesses (1.6 and 3 mm), two orientations from the injection molding direction (0° and 90°), and three load rations (−0.5, 0.1, 0.5) were investigated. A new fatigue parameter, called alternating energy density (AED), was presented; its ability to correlate the fatigue tests results was compared to other known fatigue parameters—cyclic mean strain rate and cyclic creep energy density. All the fatigue parameters were found to be independent of specimen thickness. Furthermore, the prediction of the fatigue lifetime based on AED showed greater accuracy with respect to the other known investigated methods. AED could thus be used for accurate and efficient lifetime prediction of SFRPs.

KEYWORDS
anisotropy, fatigue parameter, load ratio, short fiber-reinforced thermoplastic, thickness

Highlights

- A new unifying fatigue parameter for SFRPs called AED is proposed.
- AED proved higher unifying capabilities than other known methods.
- A new SFRP fatigue database including thickness, orientation, and load ratio is provided.

1 | INTRODUCTION

Increasingly restrictive regulations concerning global warming and greenhouse emissions have forced car manufacturers to prioritize the development of fuel-efficient and lightweight vehicles. Lightweight design and wide application of reinforced plastic materials, such as short fibers reinforced polymers (SFRPs), are thus becoming of primary importance. In the design of automotive components, the use of SFRPs can offer several benefits. Their high strength-to-weight ratio can help reduce the overall weight of vehicle components, leading to an improved overall efficiency. They provide design flexibility, where molding SFRPs into complex shapes allows more freedom in the design of automotive components. Furthermore, SFRPs can provide a cost-effective solution for automotive components as they can be manufactured using low-cost molding processes.

Accurately predicting the fatigue behavior of SFRPs is essential for their successful adoption into automotive components. Predicting the fatigue behavior of SFRPs can be challenging due to several variables, including the material behavior (type of the fibers, orientation of the fibers,[1–4] matrix material, fiber-matrix interface), the inhomogeneous and anisotropic nature of the material structure (heterogeneous orientation and the three layer structure[1–6]), loading conditions (mean stress,[7–10] strain rate,[11,12] loading frequency[11]), influence of environmental effects such as temperature and humidity.[13]

Due to all the listed variables, the orientation of the fibers plays an important role. It determines the degree of anisotropy and has a crucial influence on the stress state or triaxiality and its distribution within the component. In the thickness of the specimen, the fiber orientation varies. This microstructure has been widely discussed in the literature and is commonly known as a skin-shell-core microstructure.[1,2,5] Due to the thermal shock, the skin layer is between the injected material and the mold walls. The fibers are frozen in their position and orientation, leading to randomly oriented fibers. The shell layer is the largest layer, where the shear stress of the material flow orientates the fibers in the injection molding direction. The core layer is located in the center part of the specimen. Contrary to the shell layer, the fibers here are perpendicular to the injection molding direction. This fiber orientation is due to an extensional flow during the injection molding process.[5]

As listed previously, the environmental effects and loading conditions are variables that must also be considered in the fatigue failure assessment. For example, the effect of the mean stress on the fatigue response of SFRPs was studied by Mallick and Zhou.[7] They performed tension—tension fatigue tests at different stress ratios. A significant effect on the SN diagram was observed. The fatigue strength decreased with increasing mean stress ratio. Additionally, the mean strain during the fatigue increased, which was attributed to the creep caused by constant mean stress applied during the fatigue cycles. It is concluded that the stress amplitude mean could be fitted by a parabolic relationship. The equation called modified Gerber equation appears to represent the mean stress effects well.

The influence of the loading frequency to the fatigue strength was studied by Bernasconi and Kulin.[11] Tensile-tensile fatigue tests at a frequency ranging from 1 to 4 Hz were performed. The authors concluded that an increase in frequency is related to a decrease in fatigue strength.

All these variables together increase the complexity in predicting the fatigue response of SFRP materials and components. Moreover, achieving a comprehensive characterization of an SFRP necessitates a substantial number of tests involving variations in parameters such as fiber orientation, testing temperature, load ratio, specimen thickness, among others. Therefore, it becomes crucial to identify a fatigue parameter capable of correlating the experimental fatigue data. Such a parameter can be experimentally determined for a specific testing configuration. Together with a constitutive model describing the cyclic behavior implemented in a finite element tool, an accurate lifetime prediction for a component could be performed. This approach would significantly reduce the number of fatigue tests required for a complete characterization, thereby minimizing associated costs and time requirements. To predict the fatigue response of SFRP and identify such correlating parameter, several approaches are available in the literature. These approaches can be classified in various categories. The first category comprises the stress-based approaches where the stress components are the inputs. The failure parameter is determined by normalizing the operating stress by the ultimate tensile stress results obtained from quasi-static (q.s.) uniaxial tensile tests.[1,6] This improved parameter has been found to give good results in predicting material failure under cyclic loading. Additionally, using this parameter does not require extensive experimental testing of the material under cyclic loading conditions, which can be time-consuming and expensive. The limitation of stress-based approaches is that a single set of parameters cannot fully describe the influence of the load ratio. To address this limitation, the model needs to include additional parameters and functions that can capture the material's behavior under various load ratios, effects of ratcheting, and cyclic creep failure.[7,12]

Part of the second category of failure prediction are parameters based on strain and parameters based on the energy. The cyclic quantities used for the failure

prediction are typically calculated during cyclic loading in the stationary state.[14,15] The evolution of these quantities such as secant modulus, cyclic energy density, hysteresis energy density, and dissipated energy density are stabilized. The fatigue prediction parameters such as cyclic creep increment,[3] elastic strain energy,[16,17] and dissipated energy[18–21] are typically based on one of the mentioned cyclic quantities. The fatigue prediction, based on the mentioned parameters, is quite good and it was found that the data was independent of the orientation and environmental conditions. A limitation for the mentioned parameters is their ability to describe negative and positive load ratios. This limitation is in the nature of the mentioned parameters. For example, a fatigue failure prediction parameter based on the creep increment will not be able to describe negative load ratios (no creep occurs), while parameters based on the cyclic loop will fail to describe high load ratios.

Raphael et al.[22] proposed the strategy for mixed fatigue prediction parameters. The approach was to combine the hysteresis energy density and the cyclic mean strain rate. The hysteresis energy density was able to unify results for the negative load ratios and, on the other hand, the cyclic mean strain rate for positive load ratios. To optimize the transition between negative and positive load ratios, Raphael et al.[22] introduced a second variant of the previous fatigue failure parameter where a weight function was used. This enabled a smooth transition between the areas governed by the cyclic mean strain rate and the hysteresis energy density. An increase in accuracy (scatter band 3) in fatigue failure prediction from 84% to 92% could be established.

Santharam et al.,[13] after an intensive study of different fatigue failure parameters, applied the strategy to combine two fatigue failure parameters. They proposed two energy-based mixed parameters. The first fatigue failure parameter combines the creep energy density and the hysteresis energy density. The second variant combines the creep energy density and the cyclic energy density. The advantage of the second variant was that the cyclic energy density, compared to the hysteresis energy density, requires simpler mechanical models for the calculation. This approach enables an improvement in the fatigue failure prediction. The database took into account the influence of the fiber orientation, stress ratio, and environmental conditions. The mentioned studies show that there is a requirement of a fatigue failure method, which is able to predict the fatigue response independently of the influencing parameters (fiber orientation, load ratio, environmental conditions). However, none of the above-mentioned authors[13,22] considered the influence of the wall thickness of the specimens on the fatigue performance of SFRPs.

In this investigation, an extensive database of fatigue data was created and evaluated, and the evolution of different mechanical properties, such as cyclic mean strain rate and energy-based quantities, were monitored. Based on these results, a modified different fatigue clustering parameter for fatigue curves of SFRPs was identified.

The paper is organized as follows—Section 2 describes the material, specimens, and testing conditions, as well as the experimental procedures used in this study. In addition, the cyclic mechanical characteristics (cyclic mean strain rate, cyclic creep energy density, and alternating energy density) observed during the tests are mentioned. Section 3 illustrates the evolution of these parameters during the fatigue testing and provides a summary of the fatigue endurance determined for the tested material. Furthermore, q.s. tests were conducted and the microstructure of 1.6 and 3 mm plates was compared and discussed. In Section 4, fatigue failure parameters from the literature are presented together with a new alternating energy based fatigue parameter. Finally, the performance of the different fatigue failure parameters is discussed.

2 | MATERIAL AND METHODS

2.1 | Material and specimens manufacturing

The material under investigation is a PA6T/6I, filled with 50% weight short glass fibers, supplied under the trade name of Ultramid® Advanced T1000HG10 by BASF SE.[23] To investigate the influence of the thickness in combination with the fibers orientation on the mechanical properties, dog bone specimens were extracted from injection molded plates with two different thicknesses t (1.6 and 3 mm). One specimen per plate was machined out by milling at 0°and 90° with respect to the main flow direction as shown in Figure 1A. The shape of the specimens was designed with large radii to avoid failure in proximity of the grips. Figure 1B showcases the specimen's shape and dimensions.

2.2 | Experimental methods

2.2.1 | μCT measurements

Micro-computed tomography (μCT) scans were performed on Phoenix V|tome|x M300 computer tomography from Waygate Technologies[24] to measure the fiber orientation in the specimens. The tube voltage and current were 150 kV and 50 nA. A 0.5 mm aluminum filter

FIGURE 1 (A) Molded plate dimension, dog bone cutting position, and cutting sample position for fiber orientation analysis. (B) Specimen shape and dimensions. Dimensions are in (mm). [Colour figure can be viewed at wileyonlinelibrary.com]
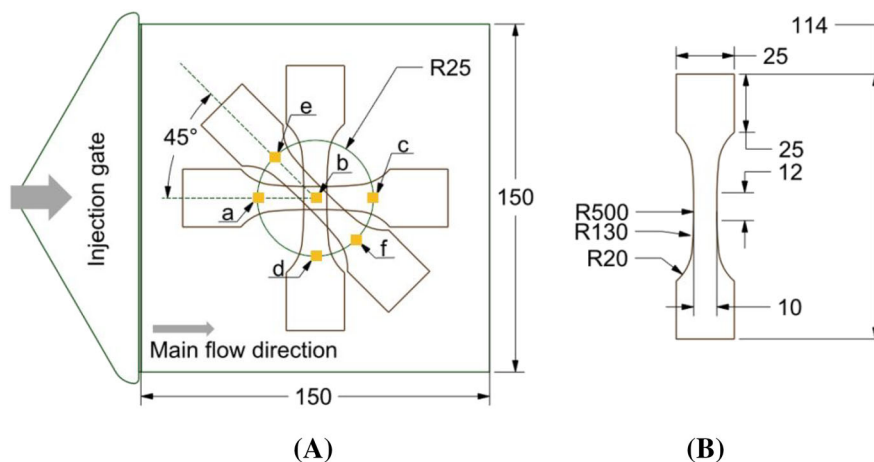
directly before the x-ray tube was used. The samples were projected on a Dynamic 41|200p + detector of 2048 × 2048 pixels, having a 200 nm pixel pitch. The 3D image was reconstructed from 2300 projections with an exposure time of 100 ms for each projection. The voxel resolution of the resulting image is 8 μm. The rendering, visualization, and determination of the fiber orientation were done in the software VG Studio Max. 3.2 from Volume Graphics.[25] Figure 2A shows the simultaneous scanning procedure of three dog bones extracted at various angles from an injection molded plate that had the same thickness. The measured area was divided in three sections to maximize the scan resolution (Figure 2B).

2.2.2 | Q.s. and fatigue testing methods

The testing campaign was performed at thyssenkrupp Presta AG. The test temperature was 80°C. The relative humidity (RH) was kept under 0.1% wt., and the specimens were sealed in individual bags after being manufactured, to prevent any change in RH prior to the experiment.

The q.s. tests were conducted with an Inspect 300-1 Hegewald and Peschke test rig. To measure the deformation of the specimens during the q.s. experiments, a 3D optical measurement system GOM ARAMIS was used. For this purpose, a random speckle pattern was applied on the specimens. Since the specimens had a gloss black finish, they were first painted with matt black. Once the paint was dry, white speckle pattern were sprayed on them. The displacement rate was 1 mm/min. Five specimens per orientations and thickness were tested. To carry out tests at 80°C, a temperature chamber equipped with a digital temperature controller was used.

For the fatigue characterization, an Instron 8802 uniaxial servo hydraulic fatigue testing machine with an environmental chamber was used. A sinusoidal load function with constant amplitude at a frequency of 4 Hz was chosen. To track the evolution of strain, a contact extensometer (Instron, model 2620-603) with a gauge length of 10 mm was utilized. During testing, a Fluke thermal camera was used to track the specimen's surface temperature. This made it possible to guarantee that the surface temperature did not exceed the chosen test temperature by more than 5°C. Complete specimen separation was the failure criterion. If a specimen did not break after 1E+6 cycles, it was considered a runout. Runouts were excluded for the computation of the parameters of the SN curve equation. Tension—tension and tension—compression tests were conducted while maintaining a constant load ratio $R_\sigma \ (= \sigma_{min}/\sigma_{max}) = 0.1$, 0.5, and −0.5, respectively. To prevent buckling during the compression phase of the tension-compression testing, a steel anti-buckling device (ABD) was used. Figure 3 shows how the ABD was installed. The ABD was not fixed within the machine clamps. Teflon sheets were installed between the specimen and the device to avoid friction effects.

2.2.3 | Mechanical quantities

Several mechanical parameters were calculated and monitored during the fatigue tests. These were evaluated from the measured strain and the nominal stress.
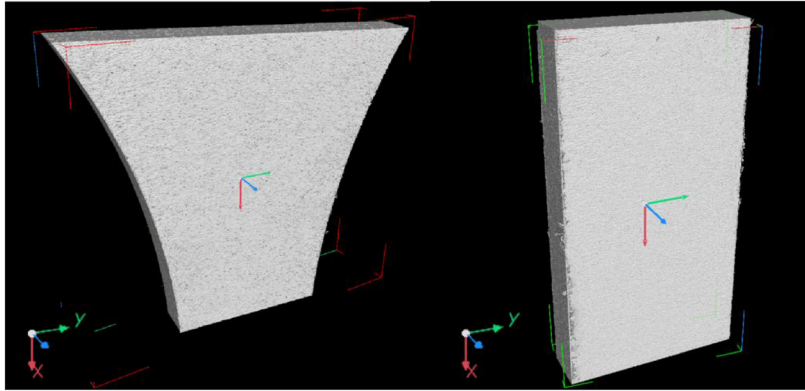
Cyclic mean strain and cyclic mean strain rate
According to previous studies,[13,22,26] the minimum and maximum strain values for each cycle were first measured. Figure 4 depicts the trend of the minimum and maximum strain during fatigue testing. Based on these values, the cyclic mean strain evolution was determined according to Equation (1).
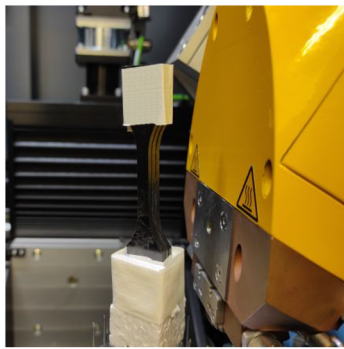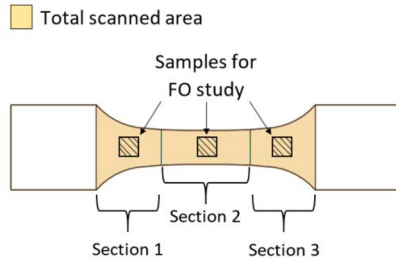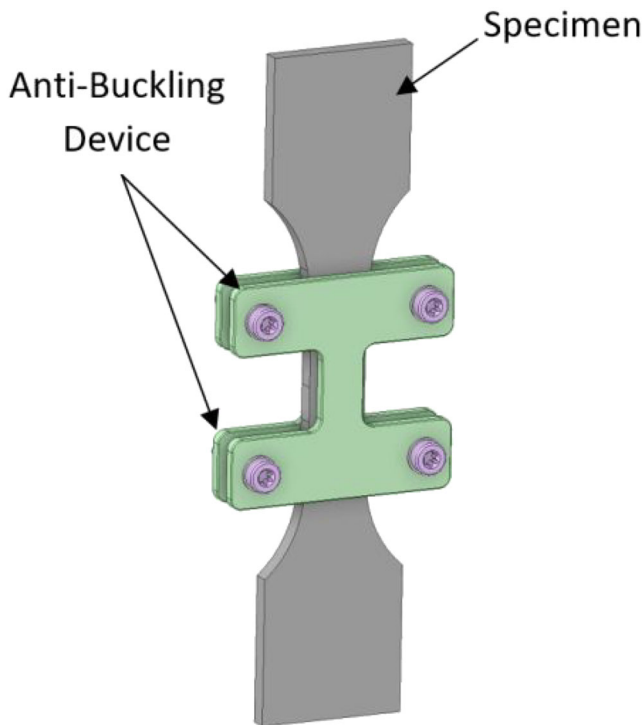
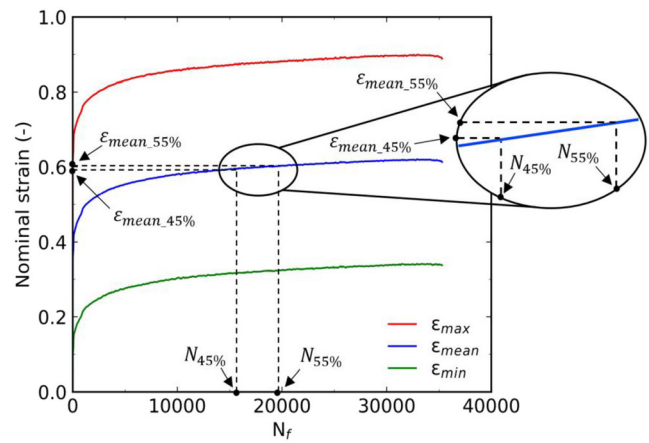FIGURE 3 Anti-buckling device and application on a dog bone a specimen. [Colour figure can be viewed at wileyonlinelibrary.com]

FIGURE 4 Axial strain evolution during a fatigue characterization. [Colour figure can be viewed at wileyonlinelibrary.com]

$$\varepsilon_{mean} = \frac{\varepsilon_{max} + \varepsilon_{min}}{2} \qquad (1)$$

The slope of the evolution of the cyclic mean strain defining the cyclic mean strain rate. Finally, the fatigue

parameter is calculated by averaging the cyclic mean strain between 45% and 55% of the lifetime (Figure 4).

Each test is assessed according to the following fatigue parameter, which is determined as follows:

$$\dot{\varepsilon}_{mean} = \frac{\varepsilon_{mean_{55\%}} - \varepsilon_{mean_{45\%}}}{N_{55\%} - N_{45\%}} frequency. \quad (2)$$

To investigate the effect of alternative intervals, we conducted a parametric study examining cyclic mean strains between 47% and 53% of the lifetime, as well as between 42% and 58% of the lifetime.

Cyclic creep energy density

The influence of the mean stress on fatigue behavior has been studied earlier.[7–10] A parameter, called cyclic creep energy density, calculated by multiplying the cyclic mean strain rate $\dot{\varepsilon}_{mean}$ with the mean stress σ_{mean} (see Equation 3) was suggested by Santharam et al.[13] It combines the cyclic energy to a parameter related to cyclic creep. The authors used the cyclic creep energy density parameter for the lifetime estimation for short fiber reinforced polymers.

$$W_{cr} = \sigma_{mean}\dot{\varepsilon}_{mean} \quad (3)$$

AED—alternating energy density

High cycle fatigue is usually caused by alternating loads in the elastic range. Due to the influence in high cycle fatigue of the alternating stresses, a modified expression of Equation (3) is proposed, named alternating energy density, which combines the cyclic mean strain rate parameter to the alternating stress. The proposed fatigue parameter, depending on the alternating stress, is expressed as follows:

$$AED = \dot{\varepsilon}_{mean}\sigma_a. \quad (4)$$

Considering the Equation (3), the cyclic creep energy density can also be expressed as follows:

$$W_{cr} = \frac{(1+R_\sigma)}{(1-R_\sigma)}\sigma_a\dot{\varepsilon}_{mean} = \frac{(1+R_\sigma)}{(1-R_\sigma)}AED. \quad (5)$$

The parameters AED and W_{cr} are interchangeable by using Equation 6:

$$AED = W_{cr}k, \quad (6)$$

where it is easy to demonstrate that the parameter k is calculated according to Equation (7).

$$k = \frac{1}{\frac{(1+R_\sigma)}{(1-R_\sigma)}} \quad (7)$$

Figure 5 shows how the parameter k varies as a function of the load ratio, R_σ. As shown, the value of k is smaller or greater than 1 if the load ratio is positive or negative, respectively.

3 | EXPERIMENTAL RESULTS

3.1 | Microstructure—Fiber orientation analysis

In Figure 6A,B, for the scanned position b (center of the plate), the measured orientation tensor components a_{xx}, a_{yy}, and a_{zz}[27] are plotted against the position through the specimen's thickness. The coordinate system considered is reported in Figure 1, that is, the x-axis is along the flow direction and z-axis points in the thickness direction of the plate. For the scanned positions b, the off-diagonal components of the matrix ranged between 0.07 and -0.03 for the 1.6 mm specimen and between 0.03 and -0.04 for the 3 mm specimen and were thus considered negligible.

According to Figure 6, the width of the non-oriented zone grows as the thickness increases and the fibers' alignment with respect to the flow direction becomes less prominent. Proportionally to the thickness of the entire specimen, the thickness of the core layer grows from around 1/8 at t = 1.6 mm to 1/4 at t = 3 mm. In the skin
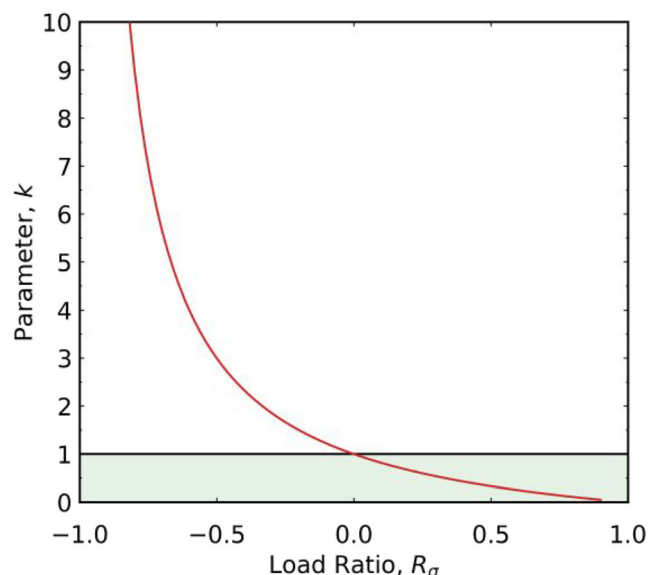

FIGURE 5 The parameter k as a function of the load ratio R_σ. [Colour figure can be viewed at wileyonlinelibrary.com]
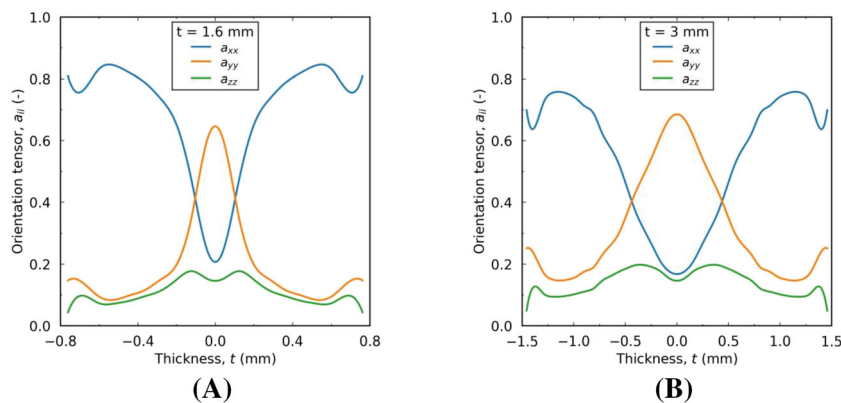
FIGURE 6 Orientation tensor distribution for (A) 1.6 mm and (B) 3 mm plate thickness. [Colour figure can be viewed at wileyonlinelibrary.com]
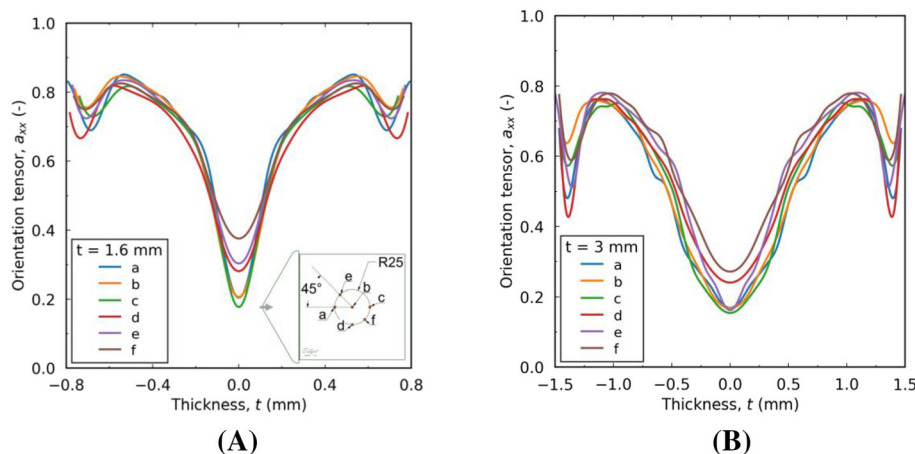

FIGURE 7 Fiber orientation tensor component in injection molding direction a_{xx} for two specimen thicknesses (A) 1.6 mm and (B) 3 mm. Six scanned locations according to Figure 1A. [Colour figure can be viewed at wileyonlinelibrary.com]

layer, contrary to the shell layer where fibers are mainly aligned in flow direction, many fibers exhibit a transverse orientation (y-axis). Similar results were reported by De Monte et al.[4]

In Figure 7A,B, the orientation tensor component a_{xx} as a function of the thickness for the 1.6 and 3 mm sample thickness is plotted, respectively.

The mean through the thickness fiber orientation tensor components a_{xx}, a_{yy}, and a_{zz} for the scanned samples are presented in Table 1A,B,C. For the two thicknesses considered, the a_{xx} displays a consistent distribution of the computed mean values at the scanned positions a, b, and c. Stadler et al.[28] made a similar consideration when the FO along the flow direction was nearly constant. For the thicknesses 1.6 and 3 mm, the range of the mean value for the orientation tensor component a_{xx}, considering all the extracted samples, was equal to 0.05 and 0.06, respectively. Comparing a_{xx}, a difference of 7.5% and 13% between scanned position c and f was detected for the 1.6 and 3 mm thickness, respectively.

Moreover, it is interesting to note that the scanned positions d, e, and f show a lower fiber alignment in the core only. An analysis of the off-diagonal matrix

components for the above mentioned scanned positions shows that the a_{xy} ranged between 0.22 and −0.03 for the 1.6 mm specimen and between 0.02 and −0.19 for the 3 mm specimen. In Figure 8, the orientation component a_{xy} for the six scanned positions is plotted.

3.2 | Q.s. and fatigue material characterization

Figure 9 compares the engineering stress versus the engineering strain behavior between the analyzed fiber orientation for the two thicknesses. The strains at failure vary between 1.5% and 2.4%, depending on the FO angle. To protect the confidentiality of the experimental results, a normalization approach for calculating stress values were used. All stresses shown in the q.s. and fatigue data are dividing by the same constant factor. This approach allowed us to report the results in a meaningful way while safeguarding the confidentiality of the experimental data.

Each curve has an initially linear strain response, which is thereafter followed by a nonlinear response until failure.

TABLE 1 Evaluation of the average a_{xx}, a_{yy}, and a_{zz} distribution for six samples, scanned at six different positions according to Figure 1(A) for two plate thicknesses.

Scanned position	Average a_{xx}		Average a_{yy}		Average a_{zz}	
	3 mm	1.6 mm	3 mm	1.6 mm	3 mm	1.6 mm
a	0.54	0.69	0.31	0.20	0.15	0.11
b	0.55	0.7	0.31	0.20	0.14	0.1
c	0.54	0.66	0.31	0.22	0.15	0.12
d	0.60	0.68	0.25	0.20	0.15	0.12
e	0.58	0.71	0.29	0.19	0.13	0.10
f	0.61	0.71	0.26	0.18	0.13	0.11
Δ	0.06	0.05	0.07	0.04	0.02	0.02

FIGURE 8 Fiber orientation tensor components a_{xy} for two specimen thicknesses (A) 1.6 mm and (B) 3 mm. Six scanned locations according to Figure 1(A). [Colour figure can be viewed at wileyonlinelibrary.com]
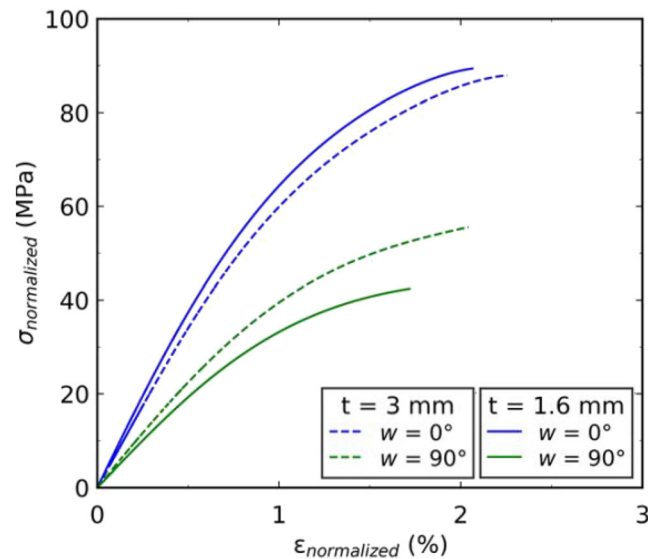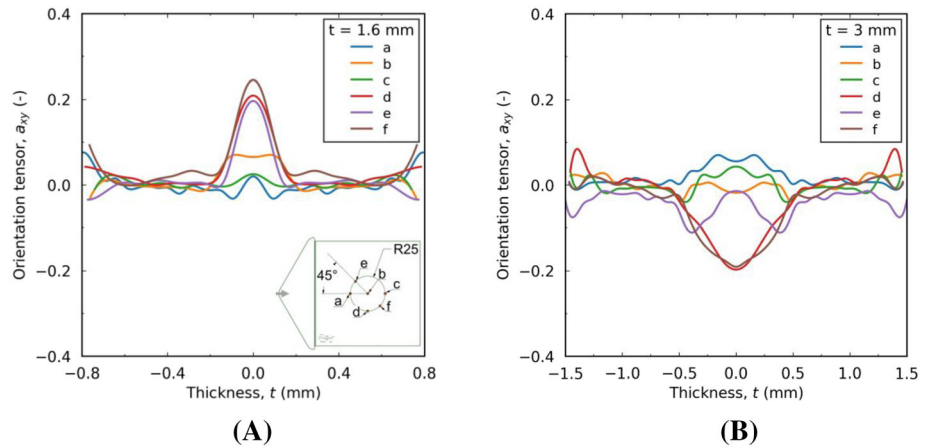

FIGURE 9 Comparison of the quasi-static (q.s.) behavior for two different orientations and two thicknesses t = 1.6 mm and t = 3 mm. [Colour figure can be viewed at wileyonlinelibrary.com]

The t = 1.6 mm specimen displays a substantial level of anisotropy. According to samples with t = 3 mm, this anisotropy becomes less noticeable as the specimen thickness increases. The varied FO distribution is considered responsible for the anisotropy's decrease with thickness. μCT measurements show that the plate with 1.6 mm thickness has well aligned fibers in main flow direction and a small relative thickness of the core, while the 3 mm plate has less aligned fibers and a larger core layer. A similar observation was reported by De Monte et al.[4] and Friedrich.[2]

Figure 10 shows the fatigue results in nominal stress amplitudes against the number of cycles to failure N_f. The number of cycles to failure N_f is interpolated using Basquin law,

$$\sigma_a = aN_f^b, \tag{8}$$

where a and b are fitting parameters.

Figure 11 shows the normalized ultimate tensile strength (UTS) and the normalized fatigue strength (residual strength at $N_f = 10E + 6$) as a function of specimen thickness with respect to the load ratios. The plotted UTS and fatigue strength for the specimen extracted at w = 0° and w = 90° were normalized by the UTS and fatigue strength of the t = 1.6 mm specimen. The influence of the thickness on fatigue strength is more

significant when compared to its influence on q.s. strength. In Figure 11A, the results for $R_\sigma = -0.5$ are plotted. The failure strength remains constant (increase of 1%) for the specimen milled at $w = 90°$. A decrease in
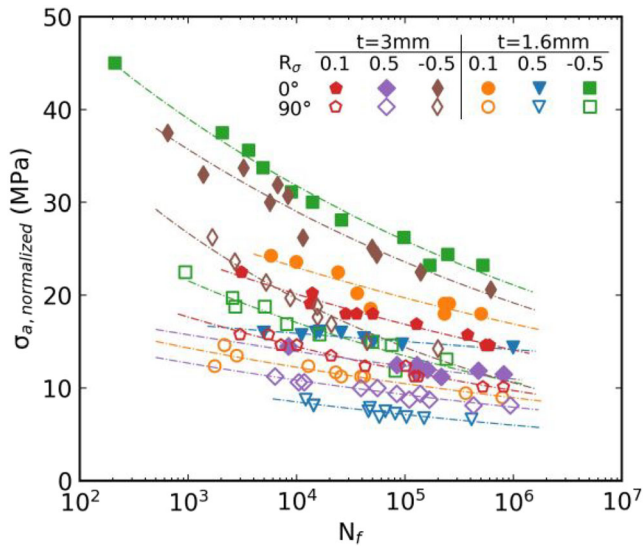

FIGURE 10 Normalized SN curves for three load ratios, two specimen thicknesses, and two orientations (dashed lines correspond to power-law fits, using Equation (7)). [Colour figure can be viewed at wileyonlinelibrary.com]

failure strength of 11% was measured for the specimens extracted in main flow direction. For the experimental tests performed with a load ratio of $R_\sigma = 0.1$ (Figure 11B), the fatigue strength increases up to 9% for the specimen extracted at $w = 90°$. On the other hand, a decrease in fatigue strength of 16% was detected for the specimen milled at $w = 0°$. Figure 11C shows an increase in fatigue strength of 33% for specimen milled at $w = 90°$. For the longitudinal extracted specimens, a 22% decrease in fatigue strength was detected.

Figure 9 have shown that the quasi-static (UTS) properties of the material depend on specimen thickness. In particular, while the t = 3 mm specimen exhibited only slight anisotropy, the t = 1.6 mm specimen demonstrated significant anisotropy. This finding is consistent with the observed microstructural changes in thicker specimens, which have a higher relative core layer and reduced fiber alignment in the main flow direction, as confirmed by μCT analysis. The influence of the thickness on the fatigue strength differs significantly from the conclusions reported for the q.s. results. Furthermore, it appears that the effect of thickness may also vary depending on the specific loading conditions, with different trends observed for tension-compression (Figure 11A) and tension-tension (Figure 11C) loading. The findings suggest that failure mechanisms vary depending on whether the
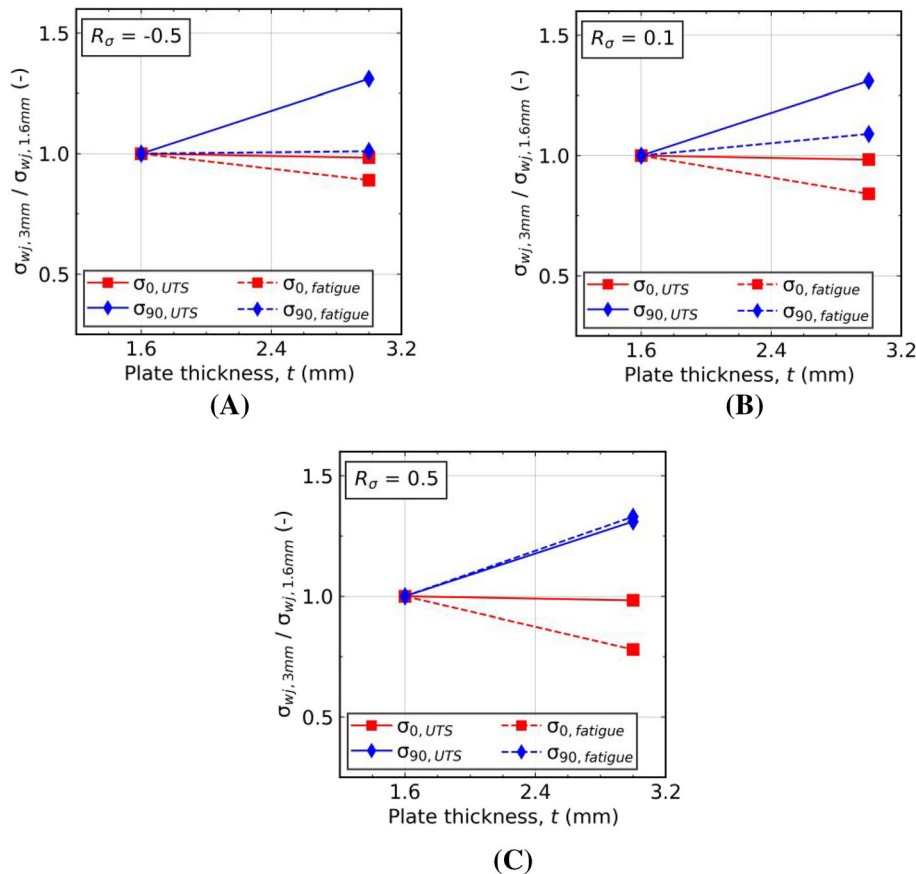

FIGURE 11 Influence of thickness on normalized fatigue strength parameters for (A) $R_\sigma = -0.5$, (B) $R_\sigma = 0.1$, and (C) $R_\sigma = 0.5$ compared to corresponding trends under quasi static loading. [Colour figure can be viewed at wileyonlinelibrary.com]

material is subjected to q.s. or cyclic loading. These observations agree with the findings reported by other authors.[6,29] As reported by Horst and Spoormaker,[30] during q.s. loading, the damage occur in the matrix, in the fibers, and at the fiber-matrix interface, while fatigue-loading causes damage mainly in the fiber-matrix interface.

4 | DISCUSSION ON THE FATIGUE PARAMETERS

4.1 | Fatigue parameters and performance

Figure 12 show the (Figure 12A) cyclic mean strain rate, the (Figure 12B) cyclic creep energy density, and the (Figure 12C) alternating energy density parameters calculated for the different specimens, respectively.

A thickness independency for the three analyzed fatigue parameters could be visually detected. Additionally, it is visible that the cyclic mean strain rate and the cyclic creep energy density fatigue parameters were able to cluster the data independently from the orientations, while they were dependent on the applied load ratio. This is coherent with the findings of previous studies.[13,22] The alternating energy density

fatigue parameter managed to group visibly almost all data regardless of the orientations, thicknesses, and load ratios.

To assess the parameter performance of clustering the data, a quantitative analysis was performed.

The following power law is used to express the relationship between the number of cycles to failure and the considered fatigue parameter:

$$Fatigue\ parameter = AN_f^q. \tag{9}$$

Equation (9) can be reformulated for the evaluation of the calculated lifetime as follows:

$$N_{f,\ calculate} = C(Fatigue\ parameter)^p, \tag{10}$$

with:

$$C = A^{-\frac{1}{q}} \quad \text{and} \quad p = \frac{1}{q}. \tag{11}$$

The coefficients, A and q, are material dependent. The coefficient set identification was carried out on the 3 mm specimen, extracted longitudinal to main flow direction, and tested with a load ratio of $R_\sigma = 0.1$. The used coefficients are reported in Table 2.
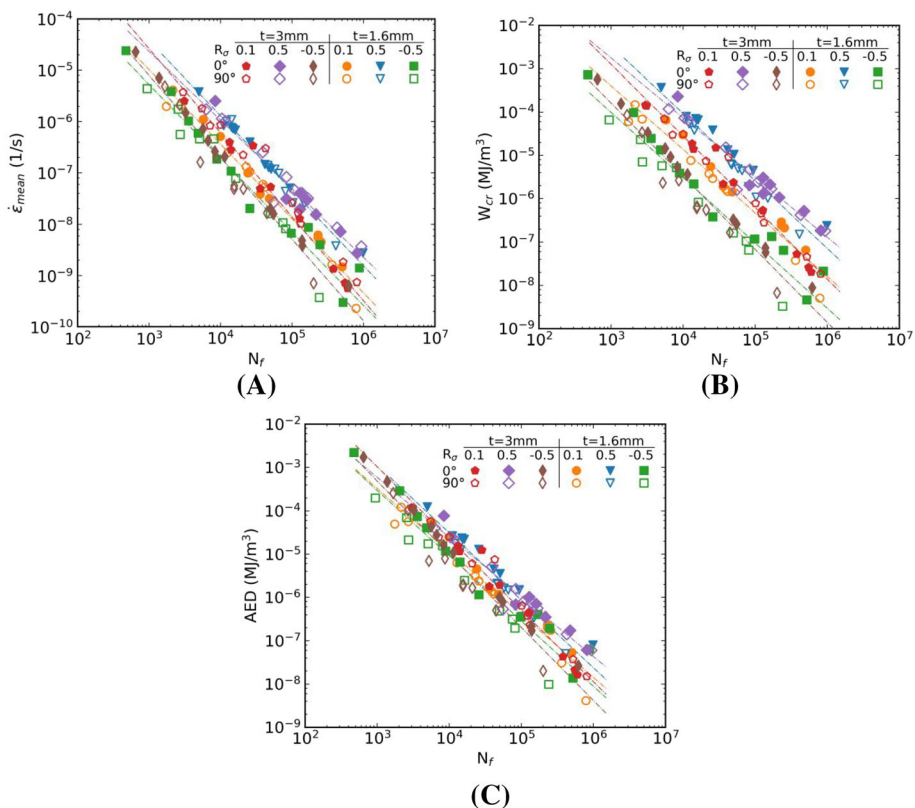

FIGURE 12 (A) Cyclic mean strain rate, (B) cyclic creep energy density, and (C) alternating energy density calculated at mid-life versus cycles to failure for the investigated load ratios, two orientations and two thicknesses (dashed lines correspond to power-law fits, using one set of parameters for each thickness and load ratio). [Colour figure can be viewed at wileyonlinelibrary.com]

To determine and compare the fatigue parameter performance, the $N_{f,calculated}$ and $N_{f,experimental}$ are compared. The estimated lifetime $N_{f,calculated}$ is calculated according to Equation (10). Scatter bands of factor two and three are marked in dashed and dotted lines, respectively.

Figure 13 compares the number of cycles to failure calculated using the cyclic mean strain rate (Figure 13A), the cyclic creep energy density (Figure 13B), and the alternating energy density (Figure 13C) material coefficients to the experimental number of cycles.

4.1.1 | Cyclic mean strain rate

By only using a single set of parameters, 69% of the calculated lifetime lays within scatter band two, whereas 93% are within scatter band three. For the tests performed at $R_\sigma = 0.5$, an underestimation can be detected. However, in the case of the negative load ratio, the $\dot{\varepsilon}_{mean}$ based fatigue parameter tends to overestimate the cycles to failure. A further investigation was performed to evaluate the dependency of the used interval for the fatigue parameter calculation. Figure 14 illustrates the cyclic mean strain rates evaluated within two additional distinct intervals: (Figure 14A) 42% to 58% and (Figure 14B) 47% to 53% of the lifetime. The results are graphically represented as a function of the cycles to failure. Detailed

TABLE 2 Material dependent coefficients for the accuracy calculation of the considered fatigue parameters.

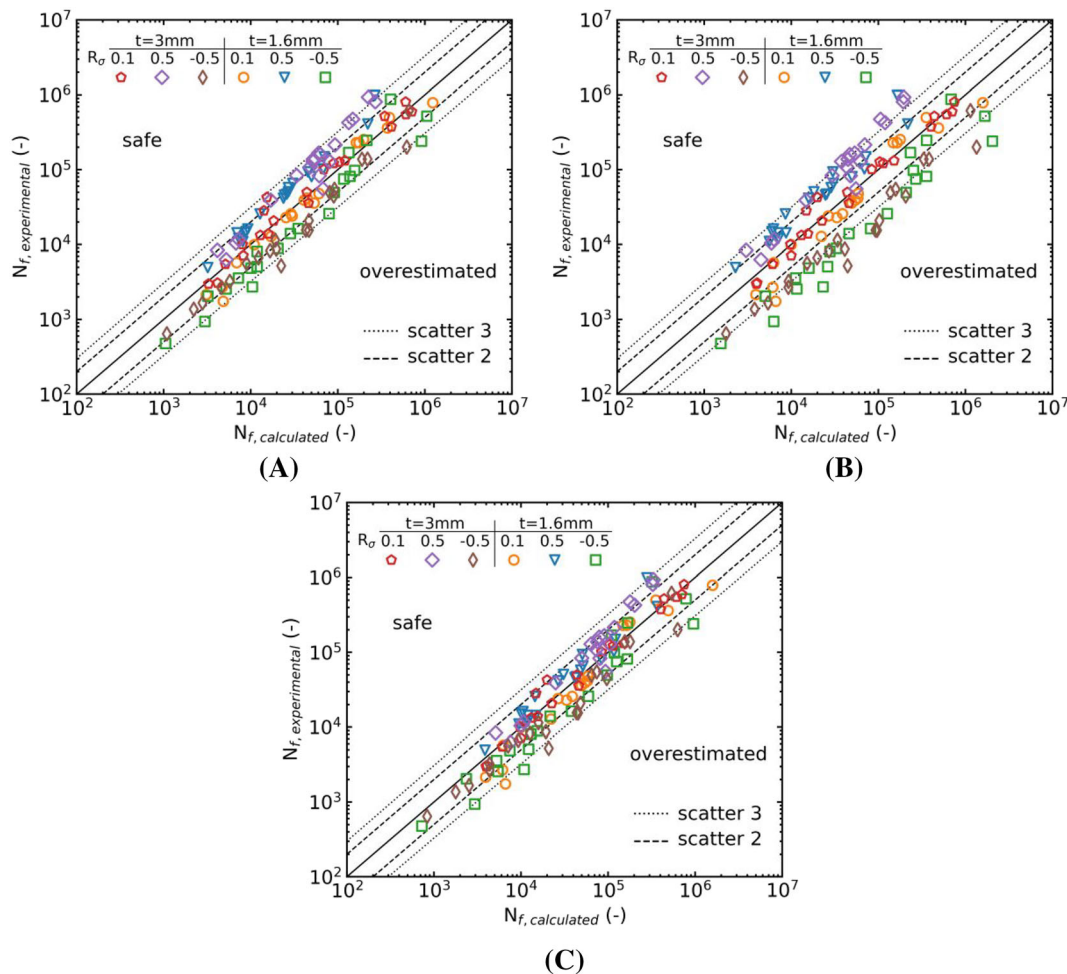| $t = 3$ mm $w = 0°$ $R_\sigma = 0.1$	Coefficients for accuracy analysis		
	$\dot{\varepsilon}_{mean}$	W_{cr}	AED
A	2.15	215.52	176.32
q	−1.637	−1.714	−1.714

FIGURE 13 Calculated fatigue lifetime using Equation (10) versus experimental number of cycle to failure based on a single set of material coefficients for (A) $\dot{\varepsilon}_{mean}$, (B) W_{cr}, and (C) AED calculated on the specimen ($t = 3$ mm) extracted longitudinal to main flow direction and tested with a load ratio of $R_\sigma = 0.1$. [Colour figure can be viewed at wileyonlinelibrary.com]
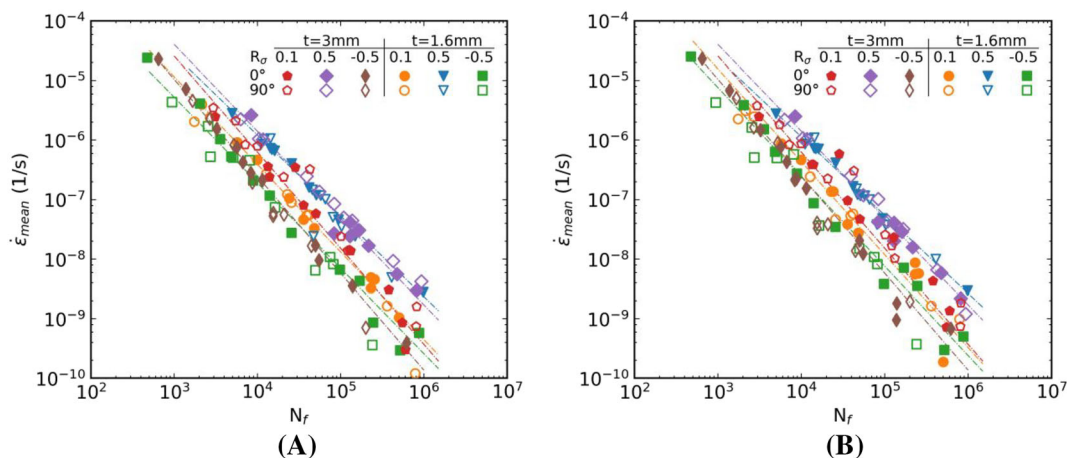
FIGURE 14 Cyclic mean strain rate evaluated between (A) 42% to 58 and (B) 47% to 53% versus cycles to failure for the investigated load ratios, two orientations, and two thicknesses (dashed lines correspond to power-law fits, using one set of parameters for each load ratio). [Colour figure can be viewed at wileyonlinelibrary.com]

TABLE 3 Accuracy results for the cyclic mean strain rate evaluated between 42%–58%, 45%–55%, and 47%–53% for scatter band two and scatter band of three.

$t = 3$ mm $w = 0°$ $R_\sigma = 0.1$	Accuracy results for different ranges		
	$\dot{\varepsilon}_{mean}$ (42%–58%)	$\dot{\varepsilon}_{mean}$ (45%–55%)	$\dot{\varepsilon}_{mean}$ (47%–53%)
Scatter 2	63%	69%	69%
Scatter 3	93%	93%	89%

accuracy findings are reported in Table 3. As shown, the 45% to 55% interval proved the highest accuracy; this is also the interval most widely used in the literature.[13,22,26] Taking these results into account, this interval was consistently applied throughout the study.

4.1.2 | Cyclic creep energy density

The accuracy analysis for the fatigue parameter based on the cyclic creep energy density yields results that are comparable to those of the cyclic mean strain rate fatigue parameter. As shown in Figure 13B, 47% of the calculated lifetime lays within scatter band two, whereas 68% are within scatter band three. However, there is a significant average discrepancy between the predicted and empirically determined cycles to failure. In comparison to the cyclic mean strain rate fatigue parameter, the tendency to overstate the negative load ratio is higher.

4.1.3 | AED—alternating energy density

In Figure 13C, the performance analysis results are presented. The quantitative performance analysis shows that 81% of the calculated lifetime lays within scatter band two, whereas 95% are within scatter band three.

4.2 | Comparison of performance

The cyclic mean strain rate ($\dot{\varepsilon}_{mean}$), the cyclic creep energy density (W_{cr}), and the alternating energy density (AED) based criteria are used to predict fatigue failure.

The newly proposed AED parameter showed higher prediction capabilities than the other tested parameters. This is explained in the following.

First of all, it must be noticed that R_σ is directly proportional to the mean stress σ_{mean} but inversely proportional to the alternating stress σ_a: for increasing R_σ, σ_{mean} increases and σ_a decreases. The opposite occurs for decreasing R_σ. Moreover, $\dot{\varepsilon}_{mean}$ is a parameter that is mainly affected by the mean stress σ_{mean}. Indeed, curves relative to higher R_σ ratios, where σ_{mean} is generally higher, show higher values of the $\dot{\varepsilon}_{mean}$ parameter (see Figure 12A).

The cyclic creep energy density (W_{cr}) multiplies $\dot{\varepsilon}_{mean}$ by σ_{mean}, thus increasing the differences between the curves and considering the effects of the mean stress twice (both via $\dot{\varepsilon}_{mean}$ and σ_{mean}) while neglecting the effects of the alternating stress σ_a. Indeed, the W_{cr} is less accurate than $\dot{\varepsilon}_{mean}$.

Conversely, the AED parameters multiplies $\dot{\varepsilon}_{mean}$ by σ_a, which is higher for lower values of R_σ and vice versa. Therefore, the curves tend to cluster rather than separate. In addition, both the effect of the mean stress (via $\dot{\varepsilon}_{mean}$)
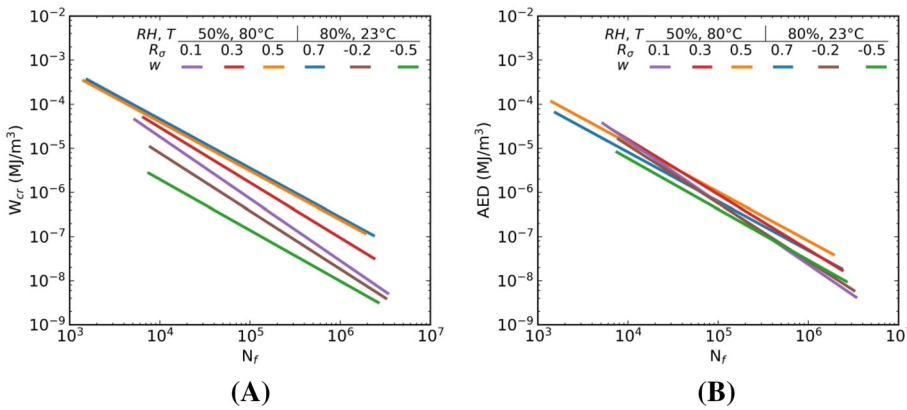
FIGURE 15 (A) Cyclic creep energy density and (B) AED—alternating energy density at for the data presented in a previous study[13] (solid lines correspond to power-law fits, using one set of parameters for each load ratio). [Colour figure can be viewed at wileyonlinelibrary.com]

and the alternating stress σ_a are considered in the AED parameter.

In conclusion, the AED parameter is more accurate than W_{cr} because it is able to take into account both the effects of the mean and alternating stress on the fatigue life of the material.

To further check the accuracy of the AED parameter, results published in a previous study[13] were used. The database was generated for dog bone specimens extracted from three different orientations ($w = 0°$, $45°$, and $90°$) to the injection molding direction and for two environmental conditions. For the environmental conditions RH50% and T = 80°C, the load ratios used were $R_\sigma = -0.5, -0.2, 0.1, 0.3, 0.5,$ and 0.7. For tests performed at T = 23°C and RH80%, the load ratios used were $R_\sigma = -0.5, -0.2,$ and 0.1. In Figure 15A, the cyclic creep energy density results are plotted against the cycles to failure N_f. The solid lines represent the power law for one load ratio, three orientations, and two environmental conditions. Even if the results were normalized, the previously presented parameter k allows us to calculate the AED independent of the real mechanical properties such as σ_a. Figure 15B shows the AED parameter calculated according to Equation (6) and Equation (7).

Data in Figure 15B are clearly more clustered. From a qualitative point of view, the fatigue parameter was able to group the data independently from parameters such as thickness, load ratio, environmental conditions, and orientation. To be able to perform an accuracy analysis on the results of a previous study,[13] the experimental results would be needed.

Based on our tests, in terms of a quantitative fatigue prediction accuracy, the alternating energy density fatigue parameter shows good results. Additionally, the application of the AED requires a minimum experimental effort.

At present, AED lacks the capability to predict SN curves. To achieve this, a constitutive model describing the cyclic behavior (see for example Launay et al.[31]) is required to evaluate the mean strain rate. Future research should prioritize the development of such a method. The input parameters for this model would include the mean strain rate, stress amplitude, and the C and p parameters (whose identification requires only one SN curve, as demonstrated in this paper). The desired output would be the number of cycles to failure.

5 | CONCLUSIONS

In this work, the fatigue behavior of a PA6T/6I-GF50 material was investigated using specimens of two different thicknesses (1.6 and 3 mm) and two orientations (0° and 90°) milled from injection molded plates. Fatigue testing was conducted under three different load ratios (-0.5, 0.1, and 0.5), monitoring the maximum and minimum strain during characterization. A microstructural evaluation of the injection molded plate and as a function of the thickness was also performed using μCT scans. Based on the presented results, the following conclusions can be drawn:

- The three fatigue failure parameters considered, namely, the cyclic mean strain rate, cyclic creep energy density, and the newly proposed AED (alternating energy density), successfully clustered the data independently of specimen thickness.
- Load ratio dependency was observed for the cyclic mean strain rate and cyclic creep energy density fatigue failure parameters.
- The AED parameter effectively grouped 95% of the data within the scatter band three. The parameter thus proved to be independent of the main fiber orientation, specimens' thickness, and load ratio.
- An accuracy comparison proved the newly proposed AED parameter to be more accurate than the other

considered parameters. This was likely due to the fact that the AED is able to consider both the effect of the mean and alternating stress or strain components.

Further investigations should focus on applying the fatigue parameter to notched specimens, multiaxial stress states, or components to determine its applicability to complex topologies. Additionally, exploring the implementation of AED in numerical methodologies using existing Finite Element tools could be a promising approach.

NOMENCLATURE

ABD	Anti-buckling device
AED	Alternating energy density
CT	Computer tomography
E	Young's modulus
$E_{Effective}$	Effective Young's modulus
FO	Fiber orientation
HCF	High cycle fatigue
k	Alternating parameter
$N_{45\%}$	Cycles to failure at 45% lifetime
$N_{55\%}$	Cycles to failure at 55% lifetime
N_f	Cycles to failure
$N_{f,calc.}$	Calculated number of cycles to failure
$N_{f,exp.}$	Experimental number of cycles to failure
q.s.	Quasi-static
RH	Relative humidity
R_σ	Load ratio
SFRP	Short fiber reinforced polymer
T	Temperature
t	Thickness
UTS	Ultimate tensile strength
W_{cr}	Cyclic creep energy density
wt.	Weight
ε	Strain
ε_{max}	Maximum strain
ε_{mean}	Mean strain
ε_{min}	Minimum strain
$\dot{\varepsilon}_{mean}$	Cyclic mean strain rate
σ	Stress
σ_a	Alternating stress
σ_{max}	Maximum stress
σ_{mean}	Mean stress
σ_{min}	Minimum stress
$\Delta\varepsilon$	Delta strain
$\Delta\sigma$	Delta stress

DATA AVAILABILITY STATEMENT

The data that support the findings of this study are available from the corresponding author upon reasonable request.

ORCID

Luca M. Martulli https://orcid.org/0000-0002-1754-9054
Andrea Bernasconi https://orcid.org/0000-0002-8611-4134

REFERENCES

1. Bernasconi A, Davoli P, Basile A, Filippi A. Effect of fibre orientation on the fatigue behaviour of a short glass fibre reinforced polyamide-6. *Int J Fatigue*. 2007;29(2):199-208.
2. Friedrich K. Microstructural efficiency and fracture toughness of short fiber/thermoplastic matrix composites. *Compos Sci Technol*. 1985;22(1):43-74.
3. Horst JJ. *Influence of fibre orientation on fatigue of short glassfibre reinforced polyamide* [Doctoral thesis]. Industrial Design Engineering, Delft University; 1997.
4. Monte MD, Moosbrugger E, Quaresimin M. Influence of temperature and thickness on the off-axis behaviour of short glass fibre reinforced polyamide 6.6 – quasi-static loading. *Compos Part Appl Sci Manuf*. 2010;41(7):859-871.
5. Bernasconi A, Cosmi F, Dreossi D. Local anisotropy analysis of injection moulded fibre reinforced polymer composites. *Compos Sci Technol*. 2008;68(12):2574-2581.
6. Monte MD, Moosbrugger E, Quaresimin M. Influence of temperature and thickness on the off-axis behaviour of short glass fibre reinforced polyamide 6.6 – cyclic loading. *Compos Part Appl Sci Manuf*. 2010;41(10):1368-1379.
7. Mallick PK, Zhou Y. Effect of mean stress on the stress-controlled fatigue of a short E-glass fiber reinforced polyamide-6,6. *Int J Fatigue*. 2004;26(9):941-946.
8. Mortazavian S, Fatemi A. Effects of mean stress and stress concentration on fatigue behavior of short fiber reinforced polymer composites. *Fatigue Fract Eng M*. 2016;39(2):149-166.
9. Sauer JA, McMaster AD, Morrow DR. Fatigue behavior of polystyrene and effect of mean stress. *J Macromol Sci Part B*. 2008;12(4):535-562.
10. Sonsino CM, Moosbrugger E. Fatigue design of highly loaded short-glass-fibre reinforced polyamide parts in engine compartments. *Int J Fatigue*. 2008;30(7):1279-1288.
11. Bernasconi A, Kulin RM. Effect of frequency upon fatigue strength of a short glass fiber reinforced polyamide 6: a superposition method based on cyclic creep parameters. *Polym Compos*. 2009;30(2):154-161.
12. Eftekhari M, Fatemi A. On the strengthening effect of increasing cycling frequency on fatigue behavior of some polymers

and their composites: experiments and modeling. *Int J Fatigue*. 2016;87:153-166.

13. Santharam P, Marco Y, Saux VL, Saux ML, Robert G, et al. Fatigue criteria for short fiber-reinforced thermoplastic validated over various fiber orientations, load ratios and environmental conditions. *Int J Fatigue*. 2020;135:105574.

14. Benoit A, Maitournam MH, Rémy L, Oger F. Cyclic behaviour of structures under thermomechanical loadings: application to exhaust manifolds. *Int J Fatigue*. 2012;38:65-74.

15. Constantinescu A, Dang Van K, Maitournam M. A unified approach for high and low cycle fatigue based on shakedown concepts. *Fatigue Fract Eng M*. 2003;26(6):561-568.

16. Klimkeit B, Castagnet S, Nadot Y, et al. Fatigue damage mechanisms in short fiber reinforced PBT+PET GF30. *Mater Sci Eng a*. 2011;528(3):1577-1588.

17. Kujawski D, Ellyin F. A unified approach to mean stress effect on fatigue threshold conditions. *Int J Fatigue*. 1995;17(2):101-106.

18. Amiable S, Chapuliot S, Constantinescu A, Fissolo A. A comparison of lifetime prediction methods for a thermal fatigue experiment. *Int J Fatigue*. 2006;28(7):692-706.

19. Jegou L, Marco Y, Le Saux V, Calloch S. Fast prediction of the Wöhler curve from heat build-up measurements on short fiber reinforced plastic. *Int J Fatigue*. 2013;47:259-267.

20. Launay A, Maitournam M, Marco Y, Raoult I. Multiaxial fatigue models for short glass fibre reinforced polyamide. Part II: fatigue life estimation. *Int J Fatigue*. 2013;47:390-406.

21. Meneghetti G, Quaresimin M. Fatigue strength assessment of a short fiber composite based on the specific heat dissipation. *Compos Part B Eng*. 2011;42(2):217-225.

22. Raphael I, Saintier N, Rolland H, Robert G, Laiarinandrasana L. A mixed strain rate and energy based fatigue criterion for short fiber reinforced thermoplastics. *Int J Fatigue*. 2019;127:131-143.

23. *BASF SE, Ultramid® advanced T1000 (PA, PPA)*. https://plastics-rubber.basf.com/global/en/performance_polymers/products/ultramid_advanced_t1000.html

24. *Waygate technologies, Phoenix micro CT scanner*. https://www.bakerhughes.com/waygate-technologies/industrial-

radiography-and-ct/phoenix-advanced-industrial-xray-and-ct/phoenix-vtomex-m-high-speed-3d-ct-scanner

25. *Volume graphics, VGSTUDIO MAX*. https://www.volumegraphics.com/de/produkte/vgsm.html

26. Gillet S, Jacopin T, Joannès S, Bedrici N, Laiarinandrasana L. Short-term creep and low cycle fatigue unified criterion for a hybridised composite material. *Int J Fatigue*. 2022;155:106571.

27. Advani SG, Tucker CL III. The use of tensors to describe and predict fiber orientation in short fiber composites. *J Rheol*. 1987;31(8):751-784.

28. Stadler G, Primetzhofer A, Pinter G, Grün F. Evaluation and consideration of local specimen material properties in lifetime prediction of short fiber-reinforced PA6T/6I. *Fatigue Fract Eng M*. 2022;45(4):980-990.

29. Lang R, Manson J, Hertzberg R. Mechanisms of fatigue fracture in short glass fibre-reinforced polymers. *J Mater Sci*. 1987;22(11):4015-4030.

30. Horst J, Spoormaker J. Fatigue fracture mechanisms and fractography of short-glassfibre-reinforced polyamide 6. *J Mater Sci*. 1997;32(14):3641-3651.

31. Launay A, Maitournam M, Marco Y, Raoult I, Szmytka F. Cyclic behaviour of short glass fibre reinforced polyamide: experimental study and constitutive equations. *Int J Plasticity*. 2011;27(8):1267-1293.